International Journal of Thermal Sciences 84 (2014) 48–61

Contents lists available at ScienceDirect

International Journal of Thermal Sciences

journal homepage: www.elsevier.com/locate/ijts

An investigation of natural convection in parallel square plates with a heated top surface by a hybrid boundary condition

Wu-Shung Fu [a,*], Wei-Hsiang Wang [a], Chung-Gang Li [b]

[a] Department of Mechanical Engineering, National Chiao Tung University, 1001 Ta Hsueh Road, Hsinchu 30010, Taiwan, ROC
[b] Complex Phenomena Unified Simulation Research Team, RIKEN, Advanced Institute for Computation Science, Kobe 650-0047, Japan

ARTICLE INFO

Article history:
Received 8 August 2013
Received in revised form
14 April 2014
Accepted 14 April 2014
Available online 2 June 2014

Keywords:
Natural convection
Parallel square plates
Neighboring open boundaries
Low speed compressible flow
Absorbing boundary condition
Modified LODI method

ABSTRACT

Natural convection in parallel squares plats with a heated top surface is investigated numerically. For solving a problem induced by different directions between the thermal diffusion and main flow streams, a hybrid boundary condition composed of the absorbing boundary condition and local one-dimensional inviscid relations (LODI) method is then adopted in artificial buffer zones. Methods of the Roe scheme, preconditioning and dual time stepping matching the Monotone Upstream-centered Schemes for Conservation Laws (MUSCL) are used to solve low speed compressible flows caused by natural convection. The results show that the hybrid boundary condition successfully prevents the rebound of heat energy from the artificial buffer zone back to the domain. The area-averaged Nusselt numbers of this study are slightly larger than those of existing experimental results, and the averaged deviation is about 10%.

1. Introduction

The clarification of flow and heat transfer mechanisms of natural convection in parallel square plates – which is often observed in many practical thermal devices such as in printed circuit board (PCB), solar cell, and thin film manufacturing chamber – is very important for both industrial applications and academic research. The existence of multiple neighboring open boundaries located at edges of parallel square plates is a unique characteristic. Important functions of the open boundary involve demarcating the inside and outside regions of the parallel square plates and then letting fluids flow into or out of the inside region, according to the corresponding boundary conditions of both regions. Within inside region, the phenomena induced by the boundary conditions of the parallel square plates are presented. The outside region lies outside of the domain, and the phenomena in it are not necessarily discussed. However, for satisfying the demands of computation processes conducted in the inside region, approximate boundary conditions are necessary for assigning in auxiliary in the outside region. It is well known that when the temperature difference of natural convection is larger than 30 K [1], the compressibility of the working fluid should be taken into consideration in order to simulate a more realistic situation. The speed of the compressible fluid induced by natural convection is much slower than that of the pressure wave caused by the compressible flow. Afterward, the motions of the compressible fluid in the inside region of the parallel square plates are inevitably polluted by reflection of the pressure wave from the open boundary that easily causes computation processes to diverge [2]. For solving the problem of pollution, a modified local one-dimensional inviscid relations (LODI) method – which is also called a non-reflecting boundary condition for a low speed compressible flow originally developed by [2] was proposed by Fu et al. [3,4] – and usage of the modified LODI method for a low speed compressible flow successfully solved one problem of a natural convection channel flow. In this problem, the open boundaries are separately located at both ends of the channel without a shared intersection area. That is, the treatment of the reflection of the pressure wave is only adopted to one direction normal to the boundary. However, in the situation of natural convection in the parallel square plates, an inside region is surrounded by four open boundaries that are mutual neighbors. Fluids are therefore able to flow into and out of the inside region diagonally. In the diagonal direction, the fluids' behaviors are not affected by any of the neighboring open boundaries that are exclusively and substantially influenced by an interaction of neighboring open boundaries. It means that the intersection region of the neighboring open boundaries that have two flowing directions should be treated.

* Corresponding author. Tel.: +886 3 5712121x55110; fax: +886 3 5735065.
E-mail address: wsfu@mail.nctu.edu.tw (W.-S. Fu).

http://dx.doi.org/10.1016/j.ijthermalsci.2014.04.009
1290-0729/

Nomenclature

A	area (m^2)
c	speed of sound (m/s)
e	internal energy (J/kg)
e_{target}	target internal energy (J/kg)
g	acceleration of gravity (m/s^2)
k	thermal conductivity (W/mK)
k_0	surrounding thermal conductivity (W/mK)
l_1	length of square plate (m)
l_2	height between square plates (m)
l_3	width of artificial buffer zone (m)
L	dimensionless Cartesian coordinates, $\sqrt{x^2+z^2}/\sqrt{2l_1^2}$
M	Mach number,
Nu	local Nusselt number defined in Eq. (61) $\mathrm{Nu} = l_2/k_0(T_H - T_0)[k(T)(\partial T/\partial y)]$
$\overline{\mathrm{Nu}}$	area-averaged Nusselt number defined in Eq. (65) $\overline{\mathrm{Nu}} = 1/A\int_A l_2/k_0(T_H - T_0)k(T)(\partial T/\partial y)dA$
P	pressure (Pa)
P_0	surrounding pressure (Pa)
Pr	Prandtl number (ν/α)
R	gas constant (J/kg/K)
Ra	Rayleigh number defined in Eq. (59) $\mathrm{Ra} = \mathrm{Pr}(g\rho_0^2(T_H - T_0)l_2^3/T_0\mu(T)^2)$
Ra^*	modified Rayleigh number defined in Eq. (60). $\mathrm{Ra}^* = \mathrm{Ra} \times l_1/l_2$
T	temperature (K)
T_0	temperature of surroundings (K)
T_H	temperature of heated top surface (K)
t	time (s)
t^*	dimensionless time, $t^* = t\mu_0/(\rho_0 l_2^2)$
u, v, w	velocities in x, y and z directions (m/s)
u_{target}, v_{target}, w_{target}	target velocities in x, y and z directions (m/s)
w_x, w_y, w_z	lengths of artificial buffer zones in x, y and z directions (m)
x, y, z	Cartesian coordinates (m)
X, Y, Z	dimensionless Cartesian coordinates, x/l_1, y/l_2 and z/l_1

Greek symbols

ρ	density (kg/m^3)
ρ_0	surrounding density (kg/m^3)
ρ_{target}	target density (kg/m^3)
μ	viscosity ($N\,s/m^2$)
μ_0	surrounding viscosity ($N\,s/m^2$)
γ	specific heat ratio

According to Yoo et al. [5] and Lodato et al. [6], the Navier–Stokes characteristic boundary conditions (NSCBC) were unavailable for the problems having neighboring open boundaries such as edge and corner boundaries. NSCBC was usually adopted for the flow being normal to the boundary plane, which meant the transverse terms were ignored in the edge and corner regions. In actuality, flow distortion and high reflection appeared when the flow crossed the boundaries along different directions. It might produce unstable and inaccurate results without considering these transverse terms at the boundary plane. Therefore, the transverse terms required a specific treatment for the computational domain of edge and corner effects. A kind of modified NSCBC then proposed by Yoo et al. [5] and Lodato et al. [6] for two-dimensional and three-dimensional approaches successfully brought a drastic reduction of flow distortion and numerical reflection even in regions of strong transverse convection. Similarly, the modified LODI method [3,4] for a low speed compressible flow mentioned above has difficulty in treating this kind of problem properly. In order to overcome the above difficulty, a modified method for three-dimensional absorbing boundary condition was proposed by Fu et al. [7] to solve the problem of natural convection of the parallel square plates with a heated bottom surface. In this method, artificial buffer zones needed to be added around the physical model. In the artificial buffer zone, two new terms of an artificial convection term and an artificial damping term were additionally added to the original governing equations, mainly to eliminate the reflection of the pressure wave from the edge of the artificial buffer zone. The numerical method for solving flow and thermal fields affected by an interaction of neighboring open boundaries was explained in detail. Related developments of the history of the absorbing boundary condition [8–14] were described. Recently, Mani [15] proposed an analysis method to optimize numerical sponge layers – which were the same as artificial buffer zones – as a non-reflective boundary treatment. Two-dimensional Euler's equations were solved, and the optimization of sponge strength and profile and also its length were obtained for a wide range of conditions in terms of Mach number.

In the previous study [7], a heated bottom surface was assigned in the physical model, and fluids were naturally sucked from its surroundings and flowed upward to impinge the top surface, which finally turned the flow direction to its surroundings. Both directions of the mainstream flow and the thermal diffusion were the same, causing the variation of thermal field to be accompanied with the variation of the flow field. Relative to the subject of [7], another important and practical subject of natural convection of parallel square plates with a heated top surface – which is also indicated in many industrial applications such as building cooling, solar cell and electric cooling – has seen little exploration. With the exception of the difficulty induced by the intersection of neighboring open boundaries described in [7], the thermal diffusion direction not always being consistent with the direction of mainstream flow is another thorny problem. These phenomena are significantly different from those of [7], causing the flow field to be complex and difficult to solve. Manca and Naradini [16] conducted an experimental work to reveal heat flow mechanisms in this subject. C type flow phenomena were visualized and empirical formula were proposed to indicate relationships between both Nusselt numbers and temperatures with Rayleigh numbers.

As a result, the study aims to investigate numerically natural convection of the parallel square plates with a heated top surface. In order to solve the problem induced by different directions between the thermal diffusion and main stream flow mentioned above, a hybrid boundary condition composed of the absorbing boundary condition and the modified LODI method [3,4] is then used. Methods of the Roe scheme, preconditioning and dual time stepping matching the Lower-upper symmetric-Gauss-Seidel (LUSGS) scheme are combined and used simultaneously for solving governing equations of the compressible flow induced by a high temperature difference. The results indicate achievements of the usage of the hybrid method composed of the absorbing boundary condition and modified LODI method to solve this kind of problem. Because of the heated top surface, distributions of local Nusselt numbers form concentric circles. The results compared with experimental results obtained by Manca and Naradini [16] are slightly larger than those of [16], and the averaged deviation is about 10%.

2. Physical model

A physical model of the three-dimensional parallel square plates mentioned above is indicated in Fig. 1. The three-dimensional parallel square plates regarded as an original domain are composed of the top surface of *abfe* and bottom surface of *cdhg*. Open boundaries of the original domain are *bfhd*, *fegh*, *eacg* and *abdc*. The length of the square plate is l_1 and the height between the two squares is l_2. The temperature of the heated top square is T_H, and the bottom surface is adiabatic. The direction of gravity is the negative y direction. Since the absorbing boundary is used, an additional zone called an artificial buffer zone is necessarily added to the original domain and indicated by dashed lines in Fig. 1. In this physical model, the direction of the normal line of the artificial buffer zone, in which the surface of $b_2b_1f_1f_0$ is the top surface and the surface of $d_2d_1h_1h_0$ is the bottom surface, directs the positive x direction. Similarly, the other three artificial buffer zones can be defined, and the three directions of the normal lines of the artificial buffer zones are the negative x direction and the positive and negative z directions, respectively. However, an intersection artificial buffer zone of neighboring artificial buffer zones can be observed at each corner such as a cubic rectangle composed of the top surface of $bb_0b_1b_2$ and the bottom surface of $dd_0d_1d_2$. The intersection artificial buffer zone includes two artificial buffer zones which have different directions of normal lines mentioned above, and the phenomena in the intersection buffer zone are naturally different from those in the artificial buffer zone described earlier. The solution methods used in the two zones are subsequently different. Therefore, the artificial buffer zone should exclude the intersection artificial buffer zone, and the residual zone – in which the surface of bff_2b_0 is the top surface and the surface of dhh_2d_0 is the bottom surface for example – is exclusively called by the artificial buffer zone afterward. The distance between the boundaries of the original domain and artificial buffer zone is l_3. The temperature and pressure outside the artificial buffer zone are $T_0 = 300$ K and $P_0 = 1$ atm, respectively.

In the previous study [7], the bottom surface is the heated surface that causes directions of both the thermal diffusion and the mainstream flow to be the same. The diffusion of the thermal energy is naturally accompanied with the mainstream flow. The artificial convection and damping terms for treating the fluid flow and the fully developed condition for treating the thermal diffusion in the artificial buffer zone are then suitable. However in this work the heated surface is the top surface that is opposite to that of [7]. Fluids close to the heated top surface are expanded by heat conduction mode and flow outward to their surroundings. Afterward, cooling fluids are sucked from surroundings via a region near the bottom surface and flow upward to supplement the vacant space due to the outward flow of fluids. Near the central low region, directions of the thermal diffusion from the top surface to the bottom surface and the mainstream flow from the bottom region to the top region are different. As a result, the usage of the fully developed condition for treating the thermal diffusion in the artificial buffer zone similar to [7] will easily cause part of the thermal energy to be rebounded from the edge of the artificial buffer zone back to the domain. These phenomena led to unreasonable results appear during the transient process. The modified LODI method used in Refs. [3,4] is then held on the edge of the artificial buffer zone to prevent computational processes polluted by the rebound of the thermal diffusion mentioned above. Both the absorbing boundary condition and the modified LODI method called the hybrid boundary condition are simultaneously held in the artificial buffer zone to investigate this kind of problem.

For facilitating the analysis, the following assumptions are made.

1. The flow is laminar flow.
2. The work fluid is ideal gas and follows the equation of the ideal gas state.
3. Radiation heat transfer is neglected.

The governing equations described in the original domain in which the parameters of viscosity and compressibility of the fluid and gravity are considered simultaneously are shown in the following equations.

$$\frac{\partial U}{\partial t}+\frac{\partial F}{\partial x}+\frac{\partial G}{\partial y}+\frac{\partial H}{\partial z}=S \tag{1}$$

$$P=\rho RT \tag{2}$$

The contents of U, F, G, H and S are separately indicated as follows.

$$\left.\begin{aligned} U &= \begin{pmatrix} \rho \\ \rho u \\ \rho v \\ \rho w \\ \rho E \end{pmatrix} \\ F &= \begin{pmatrix} \rho u \\ \rho u^2 + P - \tau_{xx} \\ \rho uv - \tau_{xy} \\ \rho uw - \tau_{xz} \\ \rho Eu + Pu - k\dfrac{\partial T}{\partial x} - u\tau_{xx} - v\tau_{xy} - w\tau_{xz} \end{pmatrix} \\ G &= \begin{pmatrix} \rho v \\ \rho u - \tau_{yx} \\ \rho v^2 + P - \tau_{yy} \\ \rho vw - \tau_{yz} \\ \rho Ev + Pv - k\dfrac{\partial T}{\partial y} - u\tau_{yx} - v\tau_{yy} - w\tau_{yz} \end{pmatrix} \\ H &= \begin{pmatrix} \rho w \\ \rho u - \tau_{zx} \\ \rho v - \tau_{zy} \\ \rho vw + P - \tau_{zz} \\ \rho Ew + Pw - k\dfrac{\partial T}{\partial z} - u\tau_{zx} - v\tau_{zy} - w\tau_{zz} \end{pmatrix} \end{aligned}\right\} \tag{3}$$

$$S = \begin{pmatrix} 0 \\ 0 \\ -(\rho-\rho_0)g \\ 0 \\ -(\rho-\rho_0)gv \end{pmatrix}$$

The viscosity and thermal conductivity of the fluid are based upon Sutherland's law and shown as follows.

$$\left.\begin{aligned}\mu(\mathrm{T}) &= \mu_0\left(\frac{\mathrm{T}}{\mathrm{T}_0}\right)^{\frac{2}{3}}\frac{T_0+110}{T+110}\\ k(T) &= \frac{\mu(T)\gamma R}{(\gamma-1)\mathrm{Pr}}\\ E &= \frac{P}{P(\gamma-1)}+\frac{1}{2}\left(u^2+v^2+w^2\right)\end{aligned}\right\} \tag{4}$$

where $\rho_0 = 1.1842\ \mathrm{kg/m^3}$, $g = 9.81\ \mathrm{m/s^2}$, $\mu_0 = 1.85\times10^{-5}\ \mathrm{Ns/m^2}$, $\gamma = 1.4$, $R = 287\ \mathrm{J/kg/K}$ and $\mathrm{Pr} = 0.72$.

As for the governing equations described in the artificial buffer zone [14], the artificial convection and damping terms are newly adopted. The function of the artificial convection term mainly accelerates outward velocities of fluids through the artificial buffer zone to reach a high speed that reaches near-supersonic speed at the edge of the artificial buffer zone. Moreover, the function of the artificial damping term eliminates the disturbances in the artificial buffer zone. The modified LODI method is held on the outer surface of the artificial buffer zone to prevent the rebound induced by the thermal diffusion, and therefore the modified LODI method is not necessary to be described in the governing equations. Then general forms of the governing equations in the artificial buffer zone can be described as Eq. (5). Since Eq. (5) is exclusively adopted in the artificial buffer zones, the source term induced by gravity does not exist that is different from Eq. (3) described in the original domain.

$$\frac{\partial U}{\partial t}+\frac{\partial \tilde{F}}{\partial x}+\frac{\partial \tilde{G}}{\partial y}+\frac{\partial \tilde{H}}{\partial z}+\tilde{\sigma} = 0 \tag{5}$$

where

$$\left.\begin{aligned}\tilde{F} &= F+\tilde{\eta}_F, \tilde{\eta}_F = \begin{Bmatrix}\eta_x\rho\\ \eta_x\rho u\\ \eta_x\rho v\\ \eta_x\rho w\\ \eta_x\rho E\end{Bmatrix}\\ \tilde{G} &= G+\tilde{\eta}_G, \tilde{\eta}_G = \begin{Bmatrix}\eta_y\rho\\ \eta_y\rho u\\ \eta_y\rho v\\ \eta_y\rho w\\ \eta_y\rho E\end{Bmatrix}\\ \tilde{H} &= H+\tilde{\eta}_H, \tilde{\eta}_H = \begin{Bmatrix}\eta_z\rho\\ \eta_z\rho u\\ \eta_z\rho v\\ \eta_z\rho w\\ \eta_z\rho E\end{Bmatrix}\end{aligned}\right\} \tag{6}$$

and

$$\begin{aligned}\tilde{\sigma} &= \tilde{\sigma}_x+\tilde{\sigma}_y+\tilde{\sigma}_z\\ &= \begin{bmatrix}\sigma_x\left(\rho-\rho_{\mathrm{target}}\right)\\ \sigma_x\left(\rho u-\rho u_{\mathrm{target}}\right)\\ \sigma_x\left(\rho v-\rho v_{\mathrm{target}}\right)\\ \sigma_x\left(\rho w-\rho w_{\mathrm{target}}\right)\\ \sigma_x\left(e-e_{\mathrm{target}}\right)\end{bmatrix}+\begin{bmatrix}\sigma_y\left(\rho-\rho_{\mathrm{target}}\right)\\ \sigma_y\left(\rho u-\rho u_{\mathrm{target}}\right)\\ \sigma_y\left(\rho v-\rho v_{\mathrm{target}}\right)\\ \sigma_y\left(\rho w-\rho w_{\mathrm{target}}\right)\\ \sigma_y\left(e-e_{\mathrm{target}}\right)\end{bmatrix}\\ &\quad+\begin{bmatrix}\sigma_z\left(\rho-\rho_{\mathrm{target}}\right)\\ \sigma_z\left(\rho u-\rho u_{\mathrm{target}}\right)\\ \sigma_z\left(\rho v-\rho v_{\mathrm{target}}\right)\\ \sigma_z\left(\rho w-\rho w_{\mathrm{target}}\right)\\ \sigma_z\left(e-e_{\mathrm{target}}\right)\end{bmatrix}\end{aligned} \tag{7}$$

$\tilde{\eta}_F$, $\tilde{\eta}_G$ and $\tilde{\eta}_H$ are artificial convection terms, and $\tilde{\sigma}_x$, $\tilde{\sigma}_y$ and $\tilde{\sigma}_z$ are artificial damping terms. η_x, η_y and η_z included in $\tilde{\eta}_F$,$\tilde{\eta}_G$ and $\tilde{\eta}_H$ are separately shown as follows.

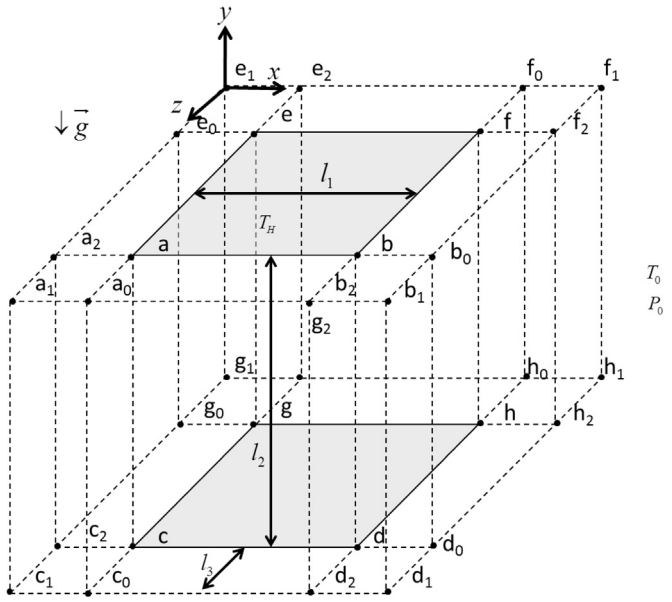

Fig. 1. Physical model of three-dimensional parallel square plates.

$$\eta_x = \begin{cases}\eta_{x0l}\left(\frac{w_{xl}-x}{w_{xl}}\right)^{\beta_{xl}} & 0\le x<w_{xl}\\ 0 & w_{xl}\le x<x_{\max}-w_{xr}\\ \eta_{x0r}\left[\frac{x-(x_{\max}-w_{xr})}{w_{xr}}\right]^{\beta_{xr}} & x_{\max}-w_{xr}\le x<x_{\max}\end{cases} \tag{8}$$

$$\eta_y = \begin{cases}\eta_{y0l}\left(\frac{w_{yl}-y}{w_{yl}}\right)^{\beta_{yl}} & 0\le y<w_{yl}\\ 0 & w_{yl}\le y<y_{\max}-w_{yr}\\ \eta_{y0r}\left[\frac{y-(y_{\max}-w_{yr})}{w_{yr}}\right]^{\beta_{yr}} & y_{\max}-w_{yr}\le y<y_{\max}\end{cases} \tag{9}$$

$$\eta_z = \begin{cases}\eta_{z0l}\left(\frac{w_{zl}-z}{w_{zl}}\right)^{\beta_{zl}} & 0\le z<w_{zl}\\ 0 & w_{zl}\le z<z_{\max}-w_{zr}\\ \eta_{z0r}\left[\frac{z-(z_{\max}-w_{zr})}{w_{zr}}\right]^{\beta_{zr}} & z_{\max}-w_{zr}\le z<z_{\max}\end{cases} \tag{10}$$

η_{x0}, η_{y0} and η_{z0} are the target velocities at the edges of the artificial buffer zones. σ_x, σ_y and σ_z are the artificial damping functions and shown as follows, respectively.

$$\sigma_x = \begin{cases}\sigma_{x0l}\left(\frac{w_{xl}-x}{w_{xl}}\right)^{\beta_{xl}} & 0\le x<w_{xl}\\ 0 & w_{xl}\le x<x_{\max}-w_{xr}\\ \sigma_{x0r}\left[\frac{x-(x_{\max}-w_{xr})}{w_{xr}}\right]^{\beta_{xr}} & x_{\max}-w_{xr}\le x<x_{\max}\end{cases} \tag{11}$$

$$\sigma_y = \begin{cases} \sigma_{y0l}\left(\frac{w_{yl}-x}{w_{yl}}\right)^{\beta_{yl}} & 0 \le y < w_{yl} \\ 0 & w_{yl} \le y < y_{\max} - w_{yr} \\ \sigma_{y0r}\left[\frac{x-(x_{\max}-w_{yr})}{w_{yr}}\right]^{\beta_{yr}} & y_{\max} - w_{yr} \le y < y_{\max} \end{cases} \quad (12)$$

$$\sigma_z = \begin{cases} \sigma_{z0l}\left(\frac{w_{zl}-x}{w_{zl}}\right)^{\beta_{zl}} & 0 \le z < w_{zl} \\ 0 & w_{zl} \le z < z_{\max} - w_{zr} \\ \sigma_{z0r}\left[\frac{x-(x_{\max}-w_{zr})}{w_{zr}}\right]^{\beta_{zr}} & z_{\max} - w_{zr} \le z < z_{\max} \end{cases} \quad (13)$$

σ_{x0}, σ_{y0} and σ_{z0} are the target damping functions at the edges of the artificial buffer zones.

Locations of φ_0 and $\varphi_{\max}$ and lengths of $w_{\varphi l}$ and $w_{\varphi r}$ are indicated in Fig. 2, respectively. In order to keep equilibrium between the order of the acoustic wave speed and both orders of the target velocities of the artificial convection terms (Eqs. (8)–(10)) and the target damping functions of the artificial damping terms (Eqs. (11)–(13)), the process proposed by Dennis et al. [17] is executed and the order of an original acoustic wave speed is transformed into the similar order of a modified acoustic wave speed. Afterward, the new target velocities of the artificial convection terms and new target damping functions of the artificial damping terms are expressed, respectively, as follows and can be adopted in a low speed compressible flow situation.

$$\eta_{xo} = c_F\frac{\sqrt{u^2(\Theta-1)^2+4\Theta c^2}}{2} \quad (14)$$

$$\eta_{yo} = c_G\frac{\sqrt{v^2(\Theta-1)^2+4\Theta c^2}}{2} \quad (15)$$

$$\eta_{zo} = c_H\frac{\sqrt{w^2(\Theta-1)^2+4\Theta c^2}}{2} \quad (16)$$

$$\sigma_{xo} = c_x\frac{\sqrt{u^2(\Theta-1)^2+4\Theta c^2}}{2} \quad (17)$$

$$\sigma_{yo} = c_y\frac{\sqrt{v^2(\Theta-1)^2+4\Theta c^2}}{2} \quad (18)$$

$$\sigma_{zo} = c_z\frac{\sqrt{w^2(\Theta-1)^2+4\Theta c^2}}{2} \quad (19)$$

where $\Theta \approx 100M^2$ and c is the speed of the sound.

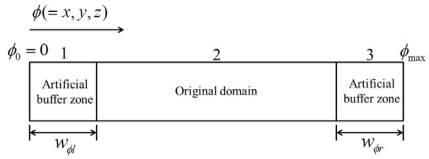

Fig. 2. The diagram of one-dimensional absorbing boundary condition.

From the previous study [7], the appropriate values of c_F, c_G, c_H, c_x, c_y, c_z are $c_F = c_G = c_H = 1.15$, $c_x = c_y = c_z = 0.05$, and $\beta = 3$, respectively.

Thus the magnitudes of the artificial convection terms will be equal to zero at the interface of the original domain and artificial buffer zones, and equal to the modified acoustic wave speed at the edges of the artificial buffer zones. Furthermore, the disturbances of the flowing fluids are gradually reduced to zero, accompanied with the location close to the edge of the artificial buffer zone.

3. Numerical method

In natural convection, the speed of the compressible fluid flow is much slower than that of the acoustic wave. The Roe Scheme [18] coordinating the preconditioning method is then adopted to resolve the governing equations shown in Eq. (1) which can be derived as the following equation and shown in Eq. (20).

$$\Gamma\frac{\partial U_p}{\partial\tau}+\frac{\partial F}{\partial x}+\frac{\partial G}{\partial y}+\frac{\partial H}{\partial z} = S \quad (20)$$

where Γ is the preconditioning matrix proposed by Weiss and Smith [19] and U_p is the primitive form of $[P, u, v, w, T]^T$.

A method of the dual time stepping is added to calculate transient states of the physical model. The derived equation is shown in Eq. (21).

$$\Gamma\frac{\partial U_p}{\partial\tau}+\frac{\partial U}{\partial t}+\frac{\partial F}{\partial x}+\frac{\partial G}{\partial y}+\frac{\partial H}{\partial z} = S \quad (21)$$

where τ is an artificial time, t is a physical time and U is the conservative form of $[\rho, \rho u, \rho v, \rho w, \rho e]^T$.

When the discretization of Eq. (21) is executed, terms of $\partial U_p/\partial\tau$ and $\partial U/\partial t$ are differentiated by a first-order forward difference and a second-order backward difference, respectively, and terms of $\partial F/\partial x$, $\partial G/\partial y$ and $\partial H/\partial z$ are differentiated by a central difference, the following equation can be obtained.

$$\Gamma\frac{U_p^{k+1}-U_p^k}{\Delta\tau}+\frac{3U^{n+1}-4U^n+U^{n-1}}{2\Delta t}+\frac{1}{\Delta x}\left(F^{k+1}_{i+\frac{1}{2},j,k}-F^{k+1}_{i-\frac{1}{2},j,k}\right)+\frac{1}{\Delta y}\left(G^{k+1}_{i,j+\frac{1}{2},k}-G^{k+1}_{i,j-\frac{1}{2},k}\right)+\frac{1}{\Delta z}\left(H^{k+1}_{i,j,k+\frac{1}{2}}-H^{k+1}_{i,j,k-\frac{1}{2}}\right) = S \quad (22)$$

Terms of U^{k+1} and F^{k+1} in Eq. (22) are necessary to be linearized and expressed as follows.

$$U^{k+1} = U^k + M\Delta U_p \quad (23)$$

$$F^{k+1} = F^k + A_p\Delta U_p \quad (24)$$

where $A_p = \partial F/\partial U_p$ is the flux jacobian and the same methods for $B_p = \partial G/\partial U_p$ and $C_p = \partial H/\partial U_p$ are used in linearization of G^{k+1} and H^{k+1}, respectively.

Eqs. (23) and (24) are substituted into Eq. (22), the following equation is derived.

$$\left[\frac{I}{\Delta\tau}+\Gamma^{-1}M\frac{3}{2\Delta t}+\Gamma^{-1}\left(\delta_xA_p^k+\delta_yB_p^k+\delta_zC_p^k\right)\right]\Delta U_p = \Gamma^{-1}R^k \quad (25)$$

where δ_x, δ_y, and δ_z are central-difference operators and $R^k = S - \left(3U^k-4U^n+U^{n-1}\right)/2\Delta t - \left(\delta_xF^k+\delta_yG^k+\delta_zH^k\right)$

In order to solve a problem of the convergence of a low speed compressible flow, the solver of Eq. (26) is newly derived from the LUSGS implicit method originally proposed by Yoon and Jamesont [20].

$$\left.\begin{aligned} L &= -\left[\frac{1}{\Delta x}\left(A_{\mathrm{p}}^{+}\right)_{i-1,j,k}+\frac{1}{\Delta y}\left(B_{\mathrm{p}}^{+}\right)_{i,j-1,k}+\frac{1}{\Delta z}\left(C_{\mathrm{p}}^{+}\right)_{i,j,k-1}\right] \\ D &= \frac{I}{\Delta\tau}+\Gamma^{-1}M\frac{3}{2\Delta t}+\left\{\frac{1}{\Delta x}\left[\left(A_{\mathrm{p}}^{+}\right)_{i,j,k}-\left(A_{\mathrm{p}}^{-}\right)_{i,j,k}\right]+\frac{1}{\Delta y}\left[\left(B_{\mathrm{p}}^{+}\right)_{i,j,k}-\left(B_{\mathrm{p}}^{-}\right)_{i,j,k}\right]+\frac{1}{\Delta z}\left[\left(C_{\mathrm{p}}^{+}\right)_{i,j,k}-\left(C_{p}^{-}\right)_{i,j,k}\right]\right\} \\ U &= \left[\frac{1}{\Delta x}\left(A_{\mathrm{p}}^{-}\right)_{i+1,j,k}+\frac{1}{\Delta y}\left(B_{\mathrm{p}}^{-}\right)_{i,j+1,k}+\frac{1}{\Delta z}\left(C_{\mathrm{p}}^{-}\right)_{i,j,k+1}\right] \end{aligned}\right\} \tag{33}$$

$$\begin{aligned} A_{\mathrm{p}} &= \Gamma^{-1}A_{\mathrm{p}}^{k} \\ B_{\mathrm{p}} &= \Gamma^{-1}B_{\mathrm{p}}^{k} \\ C_{\mathrm{p}} &= \Gamma^{-1}C_{\mathrm{p}}^{k} \end{aligned} \tag{26}$$

A_{p}, B_{p} and C_{p} can be divided into two parts.

$$\begin{aligned} A_{\mathrm{p}} &= A_{\mathrm{p}}^{+}+A_{\mathrm{p}}^{-} \\ B_{\mathrm{p}} &= B_{\mathrm{p}}^{+}+B_{\mathrm{p}}^{-} \\ C_{\mathrm{p}} &= C_{\mathrm{p}}^{+}+C_{\mathrm{p}}^{-} \end{aligned} \tag{27}$$

where

$$\begin{aligned} A_{\mathrm{p}}^{\pm} &= \frac{1}{2}\left(A_{\mathrm{p}}\pm|\lambda_{A}|I\right) \\ B_{\mathrm{p}}^{\pm} &= \frac{1}{2}\left(B_{\mathrm{p}}\pm|\lambda_{B}|I\right) \\ C_{\mathrm{p}}^{\pm} &= \frac{1}{2}\left(C_{\mathrm{p}}\pm|\lambda_{C}|I\right) \end{aligned} \tag{28}$$

To substitute Eq. (27) into Eq. (25), the following equation is obtained.

$$\begin{aligned} &\left[\frac{I}{\Delta\tau}+\Gamma^{-1}M\frac{3}{2\Delta t}+\delta_{x}\left(A_{\mathrm{p}}^{+}+A_{\mathrm{p}}^{-}\right)+\delta_{y}\left(B_{\mathrm{p}}^{+}+B_{\mathrm{p}}^{-}\right)\right. \\ &\left.+\delta_{z}\left(C_{\mathrm{p}}^{+}+C_{\mathrm{p}}^{-}\right)\right]\Delta U_{\mathrm{p}} = \Gamma^{-1}R^{k} \end{aligned} \tag{29}$$

$\delta_{x}\left(A_{p}^{+}+A_{p}^{-}\right)$ can be derived as the following equation.

$$\delta_{x}\left(\tilde{A}_{\mathrm{p}}^{+}+\tilde{A}_{\mathrm{p}}^{-}\right) = \delta_{x}^{-}\tilde{A}_{\mathrm{p}}^{+}+\delta_{x}^{+}\tilde{A}_{\mathrm{p}}^{-} = \frac{\tilde{A}_{\mathrm{p},i}^{+}-\tilde{A}_{\mathrm{p},i-1}^{+}}{\Delta x}+\frac{\tilde{A}_{\mathrm{p},i+1}^{-}-\tilde{A}_{\mathrm{p},i}^{-}}{\Delta x} \tag{30}$$

To substitute Eq. (30) into Eq. (29), and Eq. (31) can be obtained.

$$\begin{aligned} &\left[\frac{I}{\Delta\tau}+\Gamma^{-1}M\frac{3}{2\Delta t}+\frac{\tilde{A}_{\mathrm{p},i}^{+}-\tilde{A}_{\mathrm{p},i-1}^{+}}{\Delta x}+\frac{\tilde{A}_{\mathrm{p},i+1}^{-}-\tilde{A}_{\mathrm{p},i}^{-}}{\Delta x}+\frac{\tilde{B}_{\mathrm{p},j}^{+}-\tilde{B}_{\mathrm{p},j-1}^{+}}{\Delta y}\right. \\ &\left.+\frac{\tilde{B}_{\mathrm{p},j+1}^{-}-\tilde{B}_{\mathrm{p},j}^{-}}{\Delta y}+\frac{\tilde{C}_{\mathrm{p},k}^{+}-\tilde{C}_{\mathrm{p},k-1}^{+}}{\Delta z}+\frac{\tilde{C}_{\mathrm{p},k+1}^{-}-\tilde{C}_{\mathrm{p},k}^{-}}{\Delta z}\right]\Delta U_{\mathrm{p}} = \Gamma^{-1}R^{k} \end{aligned} \tag{31}$$

Eq. (31) can be rearranged as follows.

$$(L+D+U)\Delta U_{\mathrm{p}} = \Gamma^{-1}R^{k} \tag{32}$$

where

As for the computation of $R^{k} = S-(3U^{k}-4U^{n}+U^{n-1})/2\Delta t-(\delta_{x}F^{k}+\delta_{y}G^{k}+\delta_{z}H^{k})$ in the right hand side of Eq. (32), the terms in F shown in Eq. (3) can be divided into two parts. One is an inviscid term F_{inviscid} and the other is a viscous term F_{viscous}.

$$F_{\mathrm{inviscid}}\begin{pmatrix}\rho u\\ \rho u^{2}+P\\ \rho uv\\ \rho uw\\ \rho Eu+Pu\end{pmatrix} \tag{34}$$

$$F_{\mathrm{viscous}} = \begin{pmatrix}0\\ -\tau_{xx}\\ -\tau_{xy}\\ -\tau_{xz}\\ -k\dfrac{\partial T}{\partial x}-u\tau_{xx}-v\tau_{xy}-w\tau_{xz}\end{pmatrix} \tag{35}$$

Methods of the Roe scheme and preconditioning are utilized to calculate the magnitude of F_{inviscid} at the location of $i+1/2$ between the cells for a low Mach number condition.

$$F_{\mathrm{inviscid},i+\frac{1}{2}} = \frac{1}{2}(F_{\mathrm{R}}+F_{\mathrm{L}})-\frac{1}{2}\left\{\left|\Gamma^{-1}A_{\mathrm{p}}\right|\Delta U_{\mathrm{P}}\right\} \tag{36}$$

The Monotone Upstream-centered Schemes for Conservation Laws (MUSCL) with a third order proposed by Abalakin et al. [21] is used to compute Eq. (36). A fourth order central difference is adopted to calculate the F_{viscous} and Eq. (37) can be obtained.

$$\frac{\partial u}{\partial x} = \frac{u_{i-2}-8u_{i-1}+8u_{i+1}-u_{i+2}}{12\Delta x}+o\left(\Delta x^{4}\right) \tag{37}$$

In order to explain the calculation in the artificial buffer zones and the intersection artificial buffer zones mentioned above, a one-dimensional artificial buffer zone shown in Fig. 2 is used to describe the treatment of the absorbing boundary condition. The zones of 1 and 3 are the artificial buffer zones, and the zone of 2 is the original domain. w indicates the length of the artificial buffer zone, l and r mean the left and right sides, respectively. ϕ_{0} and $\phi_{\max}$ represent the start and end locations of the total domain including the zones of 1, 2 and 3. In order to avoid the reflection of acoustic waves at

ϕ_0 and ϕ_{max} rebounding back to the zone of 2, the artificial convection term accelerates the velocities of fluids – which are in the zones of 1 and 3 and flow out of the original domain – at a high speed and that is greater than the sound speed at edges of φ_0 and φ_{max}. The artificial damping term directly multiplies the disturbances of fluid velocities with an appropriate damping function to cause the disturbances to be zero within the artificial buffer zone.

Since the phenomena in the artificial buffer zones and the intersection of artificial buffer zones mentioned above are rather different, that therefore leads to the contents of the artificial convection and damping terms in the governing equations Eq. (5) to also be different. Therefore, the governing equations of the artificial buffer zone which is orthogonal to the x direction can be expressed as follows.

$$\left.\begin{aligned} \tilde{F} &= F+\tilde{\eta}_F, \quad \tilde{\eta}_F = \begin{Bmatrix} \eta_x\rho \\ \eta_x\rho u \\ \eta_x\rho v \\ \eta_x\rho w \\ \eta_x\rho E \end{Bmatrix} \\ \tilde{G} &= G+\tilde{\eta}_G, \quad \tilde{\eta}_G = 0 \\ \tilde{H} &= H+\tilde{\eta}_H, \quad \tilde{\eta}_H = 0 \end{aligned}\right\} \tag{38}$$

$$\tilde{\sigma} = \tilde{\sigma}_x = \begin{bmatrix} \sigma_x\left(\rho-\rho_{target}\right) \\ \sigma_x\left(\rho u-\rho u_{target}\right) \\ \sigma_x\left(\rho v-\rho v_{target}\right) \\ \sigma_x\left(\rho w-\rho w_{target}\right) \\ \sigma_x\left(e-e_{target}\right) \end{bmatrix} \tag{39}$$

Governing equations of the artificial buffer zone which is orthogonal to the z direction can be expressed as follows.

$$\left.\begin{aligned} \tilde{F} &= F+\tilde{\eta}_F, \quad \tilde{\eta}_F = 0 \\ \tilde{G} &= G+\tilde{\eta}_G, \quad \tilde{\eta}_G = 0 \\ \tilde{H} &= H+\tilde{\eta}_H, \quad \tilde{\eta}_H = \begin{Bmatrix} \eta_z\rho \\ \eta_z\rho u \\ \eta_z\rho v \\ \eta_z\rho w \\ \eta_z\rho E \end{Bmatrix} \end{aligned}\right\} \tag{40}$$

$$\tilde{\sigma} = \tilde{\sigma}_z \begin{bmatrix} \sigma_z\left(\rho-\rho_{target}\right) \\ \sigma_z\left(\rho u-\rho u_{target}\right) \\ \sigma_z\left(\rho v-\rho v_{target}\right) \\ \sigma_z\left(\rho w-\rho w_{target}\right) \\ \sigma_z\left(e-e_{target}\right) \end{bmatrix} \tag{41}$$

Also, governing equations used in intersections of artificial buffer zones can be expressed as follows.

$$\left.\begin{aligned} \tilde{F} &= F+\tilde{\eta}_F, \quad \tilde{\eta}_F = \begin{Bmatrix} \eta_x\rho \\ \eta_x\rho u \\ \eta_x\rho v \\ \eta_x\rho w \\ \eta_x\rho E \end{Bmatrix} \\ \tilde{G} &= G+\tilde{\eta}_G, \quad \tilde{\eta}_G = 0 \\ \tilde{H} &= H+\tilde{\eta}_H, \quad \tilde{\eta}_H = \begin{Bmatrix} \eta_z\rho \\ \eta_z\rho u \\ \eta_z\rho v \\ \eta_z\rho w \\ \eta_z\rho E \end{Bmatrix} \end{aligned}\right\} \tag{42}$$

$$\tilde{\sigma} = \tilde{\sigma}_x+\tilde{\sigma}_z = \begin{bmatrix} \sigma_x\left(\rho-\rho_{target}\right) \\ \sigma_x\left(\rho u-\rho u_{target}\right) \\ \sigma_x\left(\rho v-\rho v_{target}\right) \\ \sigma_x\left(\rho w-\rho w_{target}\right) \\ \sigma_x\left(e-e_{target}\right) \end{bmatrix} + \begin{bmatrix} \sigma_z\left(\rho-\rho_{target}\right) \\ \sigma_z\left(\rho u-\rho u_{target}\right) \\ \sigma_z\left(\rho v-\rho v_{target}\right) \\ \sigma_z\left(\rho w-\rho w_{target}\right) \\ \sigma_z\left(e-e_{target}\right) \end{bmatrix} \tag{43}$$

The direction of the fluid flow of the artificial buffer zone should be outward relative to the original domain, and then in the zone of 1 (Fig. 2) a backward finite difference form is adopted to derive the differential form. It can be expressed as Eq. (44). Similarly, in the zone of 3 (Fig. 2) a forward finite difference form is adopted and it can be expressed as Eq. (45).

For zone of 1

$$\left.\begin{aligned} \eta_\phi\frac{\partial\rho}{\partial\phi} &= \eta_\phi\frac{\rho_i-\rho_{i-1}}{\Delta\phi} \\ \eta_\phi\frac{\partial\rho u}{\partial\phi} &= \eta_\phi\frac{\rho u_i-\rho u_{i-1}}{\Delta\phi} \\ \eta_\phi\frac{\partial\rho v}{\partial\phi} &= \eta_\phi\frac{\rho v_i-\rho v_{i-1}}{\Delta\phi} \\ \eta_\phi\frac{\partial\rho w}{\partial\phi} &= \eta_\phi\frac{\rho w_i-\rho w_{i-1}}{\Delta\phi} \\ \eta_\phi\frac{\partial\rho E}{\partial\phi} &= \eta_\phi\frac{\rho E_i-\rho E_{i-1}}{\Delta\phi} \end{aligned}\right\} \tag{44}$$

For zone of 3

$$\left.\begin{aligned} \eta_\phi\frac{\partial\rho}{\partial\phi} &= \eta_\phi\frac{\rho_i-\rho_{i+1}}{\Delta\phi} \\ \eta_\phi\frac{\partial\rho u}{\partial\phi} &= \eta_\phi\frac{\rho u_i-\rho u_{i+1}}{\Delta\phi} \\ \eta_\phi\frac{\partial\rho v}{\partial\phi} &= \eta_\phi\frac{\rho v_i-\rho v_{i+1}}{\Delta\phi} \\ \eta_\phi\frac{\partial\rho w}{\partial\phi} &= \eta_\phi\frac{\rho w_i-\rho w_{i+1}}{\Delta\phi} \\ \eta_\phi\frac{\partial\rho E}{\partial\phi} &= \eta_\phi\frac{\rho E_i-\rho E_{i+1}}{\Delta\phi} \\ \phi &= x,z \end{aligned}\right\} \tag{45}$$

Eqs. (44) and (45) are adopted for the artificial buffer zones of the directions of x and z, respectively. For the intersection artificial buffer zone, the finite difference derived in the x direction and the finite difference derived in the z direction should be considered simultaneously.

In order to solve the results of the original domain and artificial buffer zone, Eqs. (1) and (5) are combined, and the integration of the governing equations can be indicated as follows.

$$\frac{\partial U}{\partial t}+\frac{\partial\tilde{F}}{\partial x}+\frac{\partial\tilde{G}}{\partial y}+\frac{\partial\tilde{H}}{\partial z}+\tilde{\sigma}+S = 0 \tag{46}$$

In the subject of natural convection of parallel square plates with a heated top surface studied in this work, the thermal diffusion direction is not always consistent with the direction of main stream flow induced by natural convection that causes the phenomena in the original physical domain to be affected by the artificial thermal field in the artificial buffer zone. In consequence, the modified LODI method used in [3,4] is necessary to be additionally added at the boundary of the artificial buffer zone, in order to prevent the thermal energy to rebound back to the original physical domain. In order to clearly explain the method, the following local

one-dimensional Navier–Stokes equation is adopted to describe the details.

$$\Gamma\frac{\partial U_p}{\partial\tau}+\frac{\partial F}{\partial x}=0 \tag{47}$$

To multiply Γ^{-1} on the left side of Eq. (47), $\partial F/\partial x$ can be transferred into a primitive form.

$$\frac{\partial U_p}{\partial\tau}+\Gamma^{-1}\frac{\partial F}{\partial x}=0 \tag{48}$$

The term of $\Gamma^{-1}(\partial F/\partial x)$ can be expressed as the following form further.

$$\Gamma^{-1}\frac{\partial F}{\partial x}=\Gamma^{-1}\frac{\partial F}{\partial U_p}\frac{\partial U_p}{\partial x}=\Gamma^{-1}A_p\frac{\partial U_p}{\partial x} \tag{49}$$

To substitute Eq. (49) into Eq. (47), the following equation can be obtained based on the primitive form.

$$\frac{\partial U_p}{\partial\tau}+\Gamma^{-1}A_p\frac{\partial U_p}{\partial x}=0 \tag{50}$$

A similar transformation of the term of $\Gamma^{-1}A_p$ is executed to obtain the characteristic velocities of the open boundaries.

$$\Gamma^{-1}A_p=K\lambda K^{-1} \tag{51}$$

where K is an eigenvector, λ are eigenvalues of the term of $\Gamma^{-1}A_p$, as well λ are characteristic velocities at the boundary. According to Dennis et al. [17], to transform the orders of u (original flow speed) and c (original acoustic wave speed) into the similar orders of u' (modified flow speed) and c' (modified acoustic wave speed), the following equation is obtained.

$$\lambda=\begin{pmatrix}\lambda_1\\ \lambda_2\\ \lambda_3\\ \lambda_4\\ \lambda_5\end{pmatrix}=\begin{pmatrix}u\\ u\\ u\\ u'+c'\\ u'-c'\end{pmatrix} \tag{52}$$

where $u'=(\Theta+1)u/2$, $c'=\sqrt{u^2(\Theta-1)^2+4\Theta c^2}/2$ and $\Theta\approx 100M^2$. Let

$$L=\lambda K^{-1}(\partial U_p/\partial x) \tag{53}$$

The contents of the term of L are

$$L\begin{pmatrix}L_1\\ L_2\\ L_3\\ L_4\\ L_5\end{pmatrix}=\begin{pmatrix}u\dfrac{\partial T}{\partial x}+\dfrac{1}{\rho\gamma}\left(\dfrac{\partial P}{\partial x}-\gamma\dfrac{\partial P}{\partial x}\right)\\ u\dfrac{\partial w}{\partial x}\\ u\left(-\dfrac{\partial v}{\partial x}\right)\\ (u'+c')\left[\dfrac{\partial P}{\partial x}-\rho(u'-c'-u)\dfrac{\partial u}{\partial x}\right]\\ (u'+c')\left[\dfrac{\partial P}{\partial x}-\rho(u'-c'-u)\dfrac{\partial u}{\partial x}\right]\end{pmatrix} \tag{54}$$

The physical meaning of the term of L is the magnitude of wave amplitude with time variation.

Based on the characteristic velocities Eq. (52), the propagation speeds of L_1, L_2, L_3, L_4 and L_5 are u, u, u, $u'+c'$ and $u'-c'$, respectively. To substitute Eq. (53) into Eq. (54), Eq. (55) can be obtained.

$$\frac{\partial U_p}{\partial\tau}+KL=0 \tag{55}$$

To derive Eq. (55), the equations of pressure, velocities and temperature through the open boundary are obtained, respectively.

$$\begin{aligned}&\frac{\partial p}{\partial\tau}+\frac{1}{2c'}[L_4(u'+c'-u)-L_5(u'-c'-u)]=0\\ &\frac{\partial u}{\partial\tau}+\frac{1}{2\rho c'}(L_4-L_5)=0\\ &\frac{\partial v}{\partial\tau}-L_3=0\\ &\frac{\partial w}{\partial\tau}+L_2=0\\ &\frac{\partial T}{\partial\tau}+L_1+\frac{1}{\rho}\frac{\gamma-1}{\gamma}\frac{1}{2c'}[L_4(u'+c'-y)-L_5(u'-c'-y)]=0\end{aligned} \tag{56}$$

The difference forms of Eq. (56) can be expressed as the following forms, respectively.

$$\begin{aligned}p^{k+1}&=p^k-\frac{\Delta t}{2\rho c'}[L_4(u'+c'-u)-L_5(u'-c'-u)]\\ u^{k+1}&=u^k-\frac{\Delta t}{2\rho c'}(L_4-L_5)\\ v^{k+1}&=v^k+L_3\Delta t\\ w^{k+1}&=w^k-L_2\Delta t\\ T^{k+1}&=T^k-L_1\Delta t+\frac{1}{\rho}\frac{\gamma+1}{\gamma}\left(p^{k+1}-p^k\right)\end{aligned} \tag{57}$$

where k is an iteration number in an artificial time.

For the calculation of the original domain, the artificial convection and damping terms are equal to zero. Oppositely, for the calculation of the domain of the artificial buffer zone, the source term is equal to zero, and the modified LODI method is adopted at the boundaries of the artificial buffer zones. Therefore, a calculation procedure is briefly described as follows.

(1) Assign the initial conditions of pressure, velocity and temperature of the artificial buffer zone, intersection artificial buffer zone and original domain. The temperature of the heated top plate is $T_H=700$ K.
(2) Use the MUSCL method to obtain the magnitude of F_R, F_L and ΔU_p.
(3) Substitute the magnitude of ΔU_p into Eq. (36) and use the Roe scheme to calculate magnitudes of inviscid terms of $F_{inviscid}$.
(4) Calculate Eq. (37) to obtain magnitudes of viscous terms and substitute into Eq. (35).
(5) Use the following Eq. (58) to solve U_p^{k+1}.

$$U_p^{k+1}=U_p^k+\Delta U_p^k \tag{58}$$

(6) Calculate Eq. (22) and examine the convergence of the computation of U_p^{k+1}. Repeat steps (2)–(5) until the convergent criteria are satisfied and the convergent magnitude of U_p^{k+1} will be regarded as that of U_p of the $(n+1)$th time step and the process proceeds to the next time step. The

convergent criteria of variables are $(\psi^{n+1}-\psi^{n})/\psi^{n+1} < 10^{-3}$, $\psi = p, u, v, w, T$.

4. Results and discussion

The height of parallel square plates is usually regarded as a characteristic length when the Rayleigh number is defined and expressed as follows.

$$\mathrm{Ra} = \mathrm{Pr}\frac{g\rho_0^2(T_\mathrm{H}-T_0)l_2^3}{T_0\mu(T)^2} \tag{59}$$

However, the area of the heated top wall affects heat transfer phenomena significantly. In order to highlight the influence of the area of the heated wall, the modified Rayleigh number Ra^* is newly defined. In the study of Manca and Nardini [16], the modified Rayleigh number is characterized by l_2/l_1. In contrast, in this study the effect of l_1/l_2 is then considered because of the difference of the physical model compared to Manca and Nardini [16]. The physical model of Manca and Nardini [16] was similar to a channel with two open-ended apertures. By increasing the length of the channel of l_1, the heated area then increase while the coolant inlet area is still not changed, and the cooling efficiency in the central region becomes lower. In this situation, the heat transfer rates may decrease, so it is reasonable to characterize the modified Rayleigh number by l_2/l_1. However in this study, the physical domain is surrounded by square plates and four open boundaries, which means by increasing the length of l_1, the coolant inlet area also be increased. To give sufficient consideration to this condition, the modified Rayleigh number is then characterized by l_1/l_2 in the following equation.

$$\mathrm{Ra}^* = \mathrm{Ra}\times\frac{l_1}{l_2} \tag{60}$$

In this work, three different values of the modified Rayleigh numbers, $\mathrm{Ra}^* = 1.72\times10^5$, $\mathrm{Ra}^* = 1.55\times10^6$ and $\mathrm{Ra}^* = 4.31\times10^6$, are investigated.

In Fig. 3, tests for determination of an appropriate length of the artificial buffer zone are executed. The definition of the local Nusselt number is shown as follows.

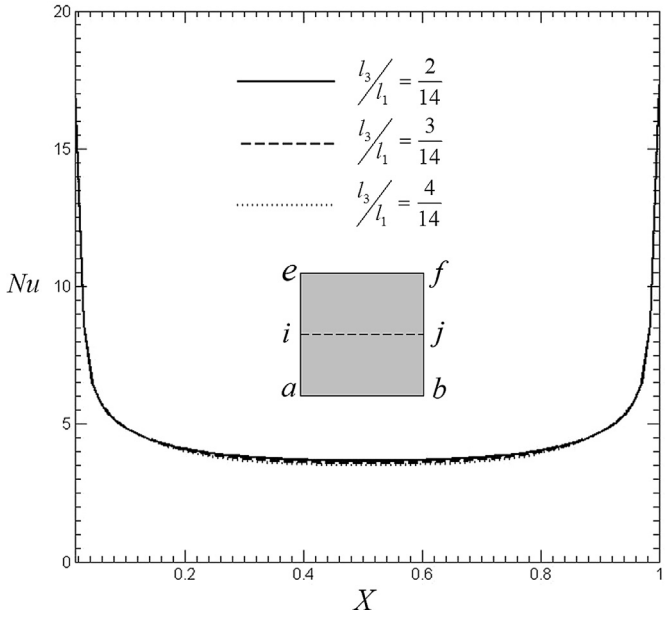

Fig. 3. Distributions of local Nusselt numbers along $\overline{ij}$ of different lengths of the artificial buffer zone under $\mathrm{Ra}^* = 1.72\times10^5$.

$$\mathrm{Nu} = \frac{l_2}{k_0(T_\mathrm{H}-T_0)}\left[k(T)\frac{\partial T}{\partial y}\right] \tag{61}$$

According to results, that the length equals to $l_3/l_1 = 3/14$ is adopted.

In Fig. 4, transient thermal fields obtained by two different methods at certain instants of transient processes are indicated, respectively. The brighter the color is, the higher the temperature is indicated. Solid lines are isothermal lines and white dashed lines are the interface between the original domain and artificial buffer zones. Shown in Fig. 4(a), the thermal field is obtained by a situation in which the absorbing boundary condition is solely adopted in the artificial buffer zone. The isothermal line between the dark grey and light black colors is immediately pushed away from the orderly arrangement of isothermal lines. This phenomenon implies the rebound of thermal energy from the boundary to occur, and it is unreasonable. For improving the phenomenon, in addition to the usage of the absorbing boundary condition, the modified LODI method [3,4] is further adopted in the artificial buffer zone. Both the absorbing boundary condition and the modified LODI method [3,4] are abbreviated as the hybrid boundary condition. It means simultaneous usage of both methods. The result obtained by the latter method is shown in Fig. 4(b). Isothermal lines are arranged in order, relative to that shown in Fig. 4(a) that indicates the correct usage of the hybrid boundary condition.

In Fig. 5, transient variations of thermal fields, velocity vectors and pressure fields during initial stages are indicated, respectively. At the beginning (Fig. 5(a)), fluids close to the heated top surface are heated by heat conduction mode and expanded, which causes the heated fluids to flow outward. The magnitude of the pressure changes from large to small, accompanied with the location from the central top region to surroundings. Parallel thermal layers on the top surface are observed that is a typical mode of heat conduction. Afterward, other fluids are sucked from their surroundings via the low region due to the heated fluids flow with a high velocity from the central top region to the surroundings mentioned above. The fluids sucked from surroundings impinge other fluids discharged from the central top region, leading to the pressure in this region to be large shown in Fig. 5(b). Both fluids coalesce and become new flow streams that flow upward, and meanwhile thermal layers begin to be distorted near the edge region. At dimensionless time $t^* = 3.14\times10^{-3}$, the upward fluids are sucked from their surroundings via the low region in the physical domain, and the phenomena of fluids that is discharged from the central top region are no longer observed. These phenomena are completely

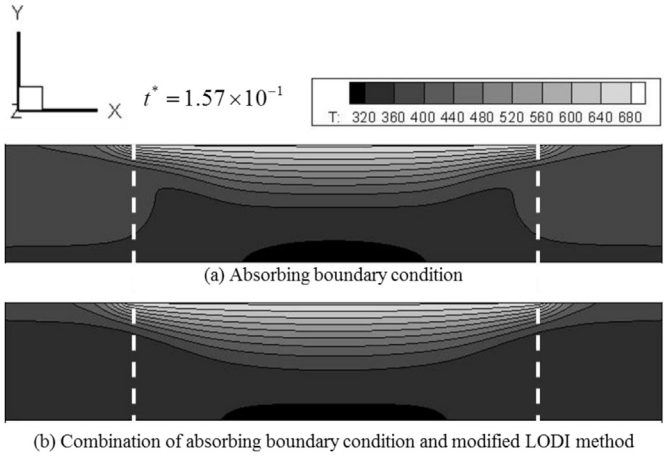

(a) Absorbing boundary condition

(b) Combination of absorbing boundary condition and modified LODI method

Fig. 4. Transient thermal fields under different boundary conditions.

affected by the natural convection mode. The magnitudes of the pressure naturally change from high to low, accompanied with the location away from the central top region. The distortion of the thermal layers becomes more apparent near the edge region.

In Fig. 6, the distributions of the velocity vectors, temperature contour and pressure contour on the central cross section of the *xy* plane under a steady state are displayed, respectively. The darker the color, the higher the temperature and pressure are indicated. The fluids move from the bottom plate to the top plate while the pressure distributions decrease from the top plate to the bottom plate. In this situation, the direction of the driving force caused by the pressure gradient is opposite to the flow direction, which appears to not be an ordinary recognition. Two reasons suggest the cause of the occurrence of the phenomenon. One is that fluids sucked from surroundings are mainly induced by strongly outward flows of fluids of which pressures are raised by the heated top surface. The other reason is caused by the influence of the buoyancy force especially in the central region. Shown in Fig. 7 are the pressures and densities at the grids of y and $y+1$ are P_y, P_{y+1} and ρ_y and ρ_{y+1}, respectively. The pressure difference at the interface of the grids of y and $y+1$ is calculated as follows.

$$\Delta P = P_{y+1} - P_y \tag{62}$$

According to the distribution of the pressure shown in Fig. 6(c), the magnitude of ΔP is positive and the flow direction ought to be downward contrary to the velocity vectors shown in Fig. 6(a). However, the direction of the buoyancy force that is calculated by the difference of both densities of ρ_0 and ρ_y is exclusively upward, and therefore the buoyancy force at the grid of $y+1$ does not affect the motion of the fluid at the grid of y. The buoyancy force f_b at the grid of y is expressed by the following equation.

$$\begin{cases} F_b = (\rho_0 - \rho_y) gV \\ f_b = F_b / A \end{cases} \tag{63}$$

As a result, the direction of the fluid is decided by the difference of both magnitudes of ΔP and f_b which are shown in Fig. 7(d). In the low region, the buoyancy force is larger than the pressure difference, and therefore the movement of fluid is upward. In the high region, although the pressure difference is larger than the buoyancy force, the suction effect induced by strongly outward flows of heated fluids mentioned above on the fluids in this high region

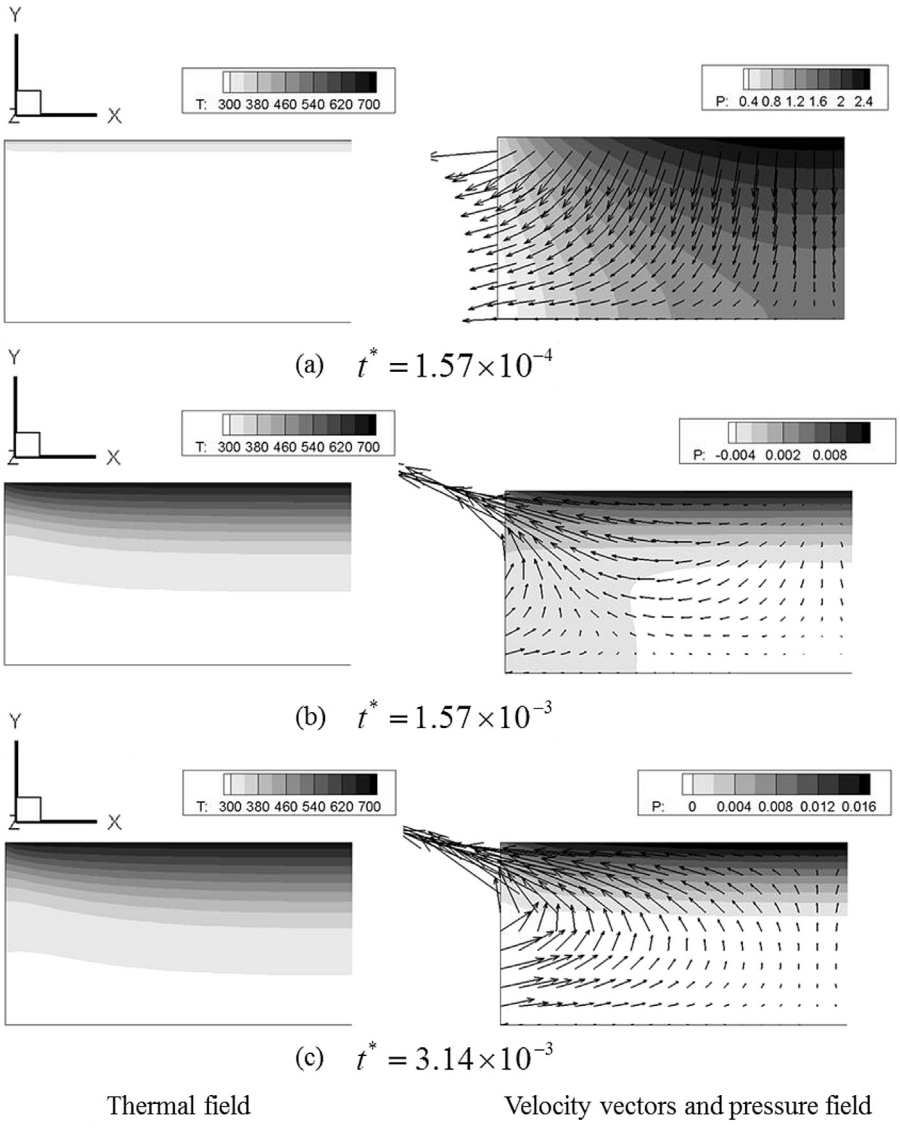

Fig. 5. Transient variations of thermal field, velocity vectors and pressure field during initial stage under $Ra^* = 1.72 \times 10^5$.

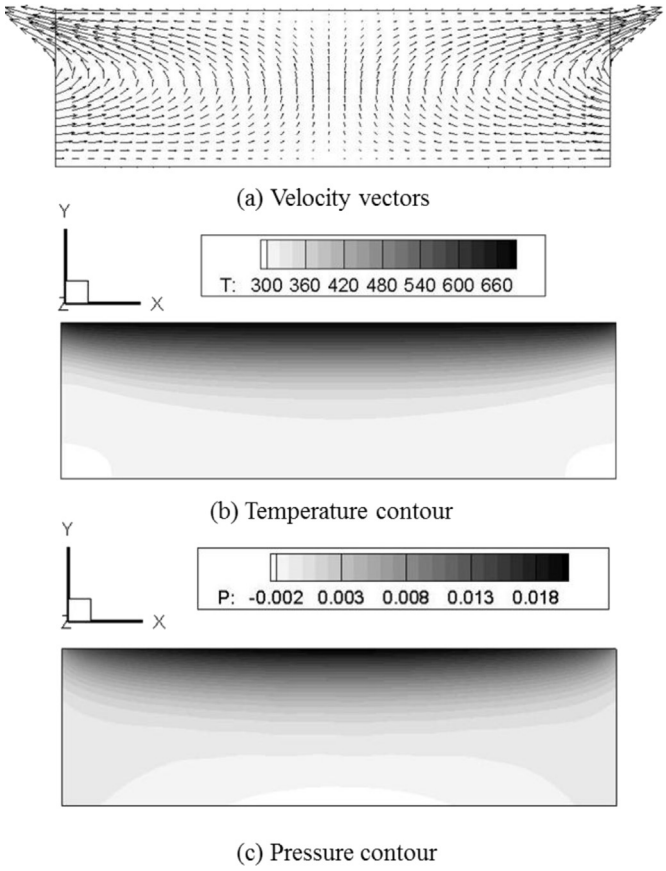

Fig. 6. Distributions of velocity vectors, temperature contour and pressure contour at a steady state under $Ra^* = 1.72 \times 10^5$.

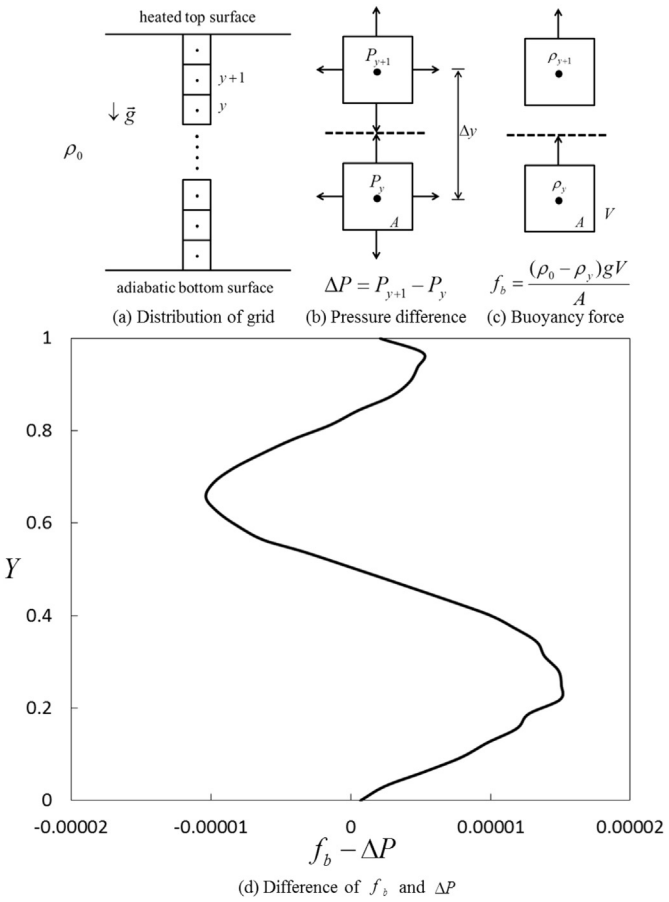

Fig. 7. Distribution of differences of ΔP and f_b under $Ra^* = 1.72 \times 10^5$.

begins to operate. The fluids are then continuously move upward and finally join into the strongly outward flows. These phenomena are quite different from those shown in the previous study [7].

Fig. 8 indicates a three-dimensional distribution of the streamlines. Due to the parallel square plates, the distribution of the streamlines displays a symmetrical shape.

In Fig. 9, the local Nusselt numbers distributed on the top surface of the central cross section under situations of three different heights are indicated, respectively. The higher the height is, the larger the space is. The distribution of the largest magnitude of the local Nusselt number is naturally the situation of $Ra^* = 4.31 \times 10^6$.

Fig. 10 reveals the distributions of the local Nusselt numbers on the central and diagonal lines of the top surface, respectively. A dimensionless parameter L means lengths of $\overline{ij}$ and $\overline{eb}$ are normalized by the length of $\overline{eb}$. Since the physical model is symmetrical, fluids from the diagonal line flow into the physical model are easily squeezed by flows distributed on both neighboring sides. Therefore, the local Nusselt numbers distributed near the edge of the diagonal line are larger than those near the edge of the central line. In the central region, both local Nusselt numbers are almost equivalent.

Local Nusselt numbers distributed on the top surface are shown in Fig. 11. The darker the color is, the smaller the magnitude displays. The fluids are heated by the top surface, and from the central region to its surroundings the fluids flow uniformly, which causes the distribution of the local Nusselt numbers to be similar to concentric circles except in the edge region. This phenomenon makes a difference compared with that of the previous study [7].

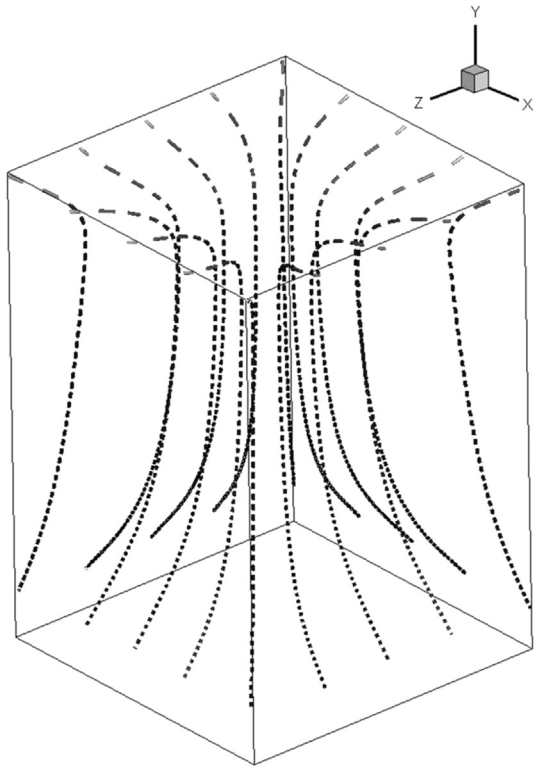

Fig. 8. Distribution of streamlines under $Ra^* = 4.31 \times 10^6$.

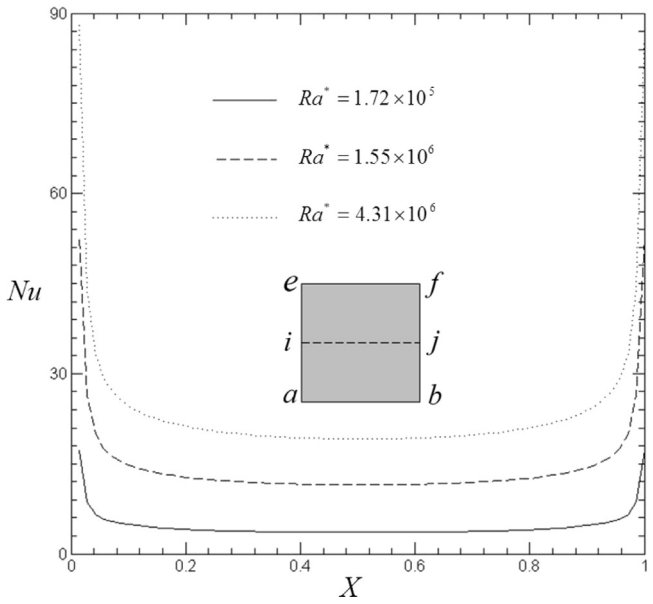

Fig. 9. Distributions of local Nusselt numbers along $\overline{ij}$ under different modified Rayleigh numbers.

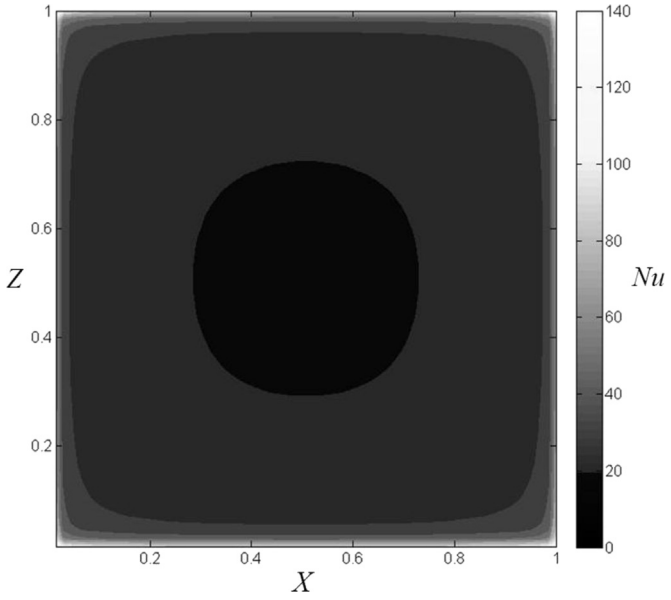

Fig. 11. Distributions of local Nusselt numbers on the heated top surface under $Ra^* = 4.31\times10^6$.

In Fig. 12, comparisons of the mass flow rates under different modified Rayleigh numbers of the previous study [7] and the present study are indicated, respectively. In the previous study [7], the heat surface is installed on the bottom surface, and the directions of the thermal diffusion and the pressure gradient that varies from the large magnitude to the small magnitude are the same. Oppositely, the heat surface of the present study is installed on the top surface, and directions of the thermal diffusion and the pressure gradient mentioned above are not always consistent. As a result, the mass flow rates through the domain of the previous study [7] are naturally larger than those of the present study. The mass flow rate is defined as follows.

$$\dot{m} = \int_{A} \rho v \cdot \mathrm{d}A \tag{64}$$

where v is the velocity flow out of the domain, and A represents the area of the open boundary.

The area-averaged Nusselt numbers of both studies are separately shown in Fig. 13. The area-averaged Nusselt number $\overline{\mathrm{Nu}}$ is defined as follows.

$$\overline{\mathrm{Nu}} = \frac{1}{A}\int_{A} \frac{l_2}{k_0(T_\mathrm{H}-T_0)}\left[k(T)\frac{\partial T}{\partial y}\right]\mathrm{d}A \tag{65}$$

Relative to the differences between both mass flow rates shown in Fig. 12, the differences of area-averaged Nusselt numbers between both studies are small. In the previous study, the fluids sucked from surroundings flow over the heated bottom surface plays a main role of heat transfer mechanism. However, in the present study, the fluids sucked from their surroundings that

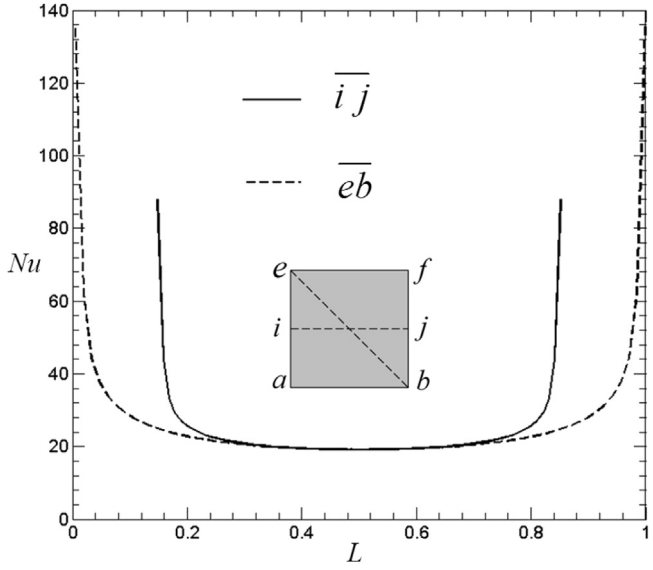

Fig. 10. Distributions of local Nusselt numbers along $\overline{ij}$ and $\overline{eb}$ on the heated top surface under $Ra^* = 4.31\times10^6$.

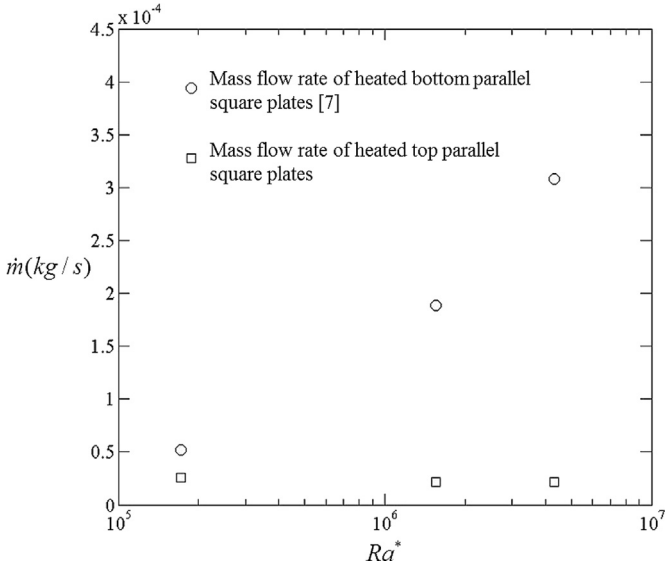

Fig. 12. Comparison of mass flow rates of present results and results of Fu et al. [7].

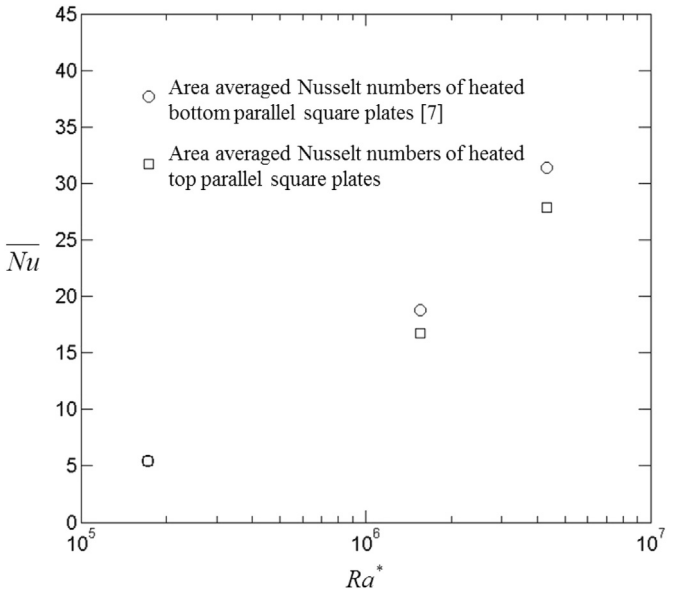

Fig. 13. Comparison of area-averaged Nusselt numbers of present results and results of Fu et al. [7].

impinge the heated top surface plays the main role of the heat transfer mechanism. The velocity fields of both studies are shown in Fig. 14(a) and (b), respectively. The heat transfer rate caused by an impingement of fluids is typically prior to that by fluids flowing over a flat plate. Consequently, although the differences shown in Fig. 12 are large, the differences of Fig. 13 became small due to different heat transfer mechanisms.

In order to compare numerical results of this work and experimental results of Manca and Naradini [16], a new model, which is the same as that of Manca and Naradini [16], is newly set and shown in Fig. 15. The parallel plates are surrounded by two solid walls ABDC and EFHG and two open boundaries BFHD and AEGC. The thermal condition of top plate ABFE is an uniform heat flux. The artificial buffer zones in $-x$ and $+x$ directions are surrounded by A_0AEE_0 and C_0CGG_0, and BB_0F_0F and DD_0H_0H, respectively. The modified LODI method is adopted at surfaces of $A_0E_0G_0C_0$ and $B_0F_0H_0D_0$. The parameters of computation are listed in Table 1.

Shown in Fig. 16, a comparison of the area-averaged Nusselt numbers of the present results and experimental results of Manca and Naradini [16] is indicated. The results show that the area-averaged Nusselt numbers of this work are slightly larger than those of [16], and the averaged deviation is about 10%.

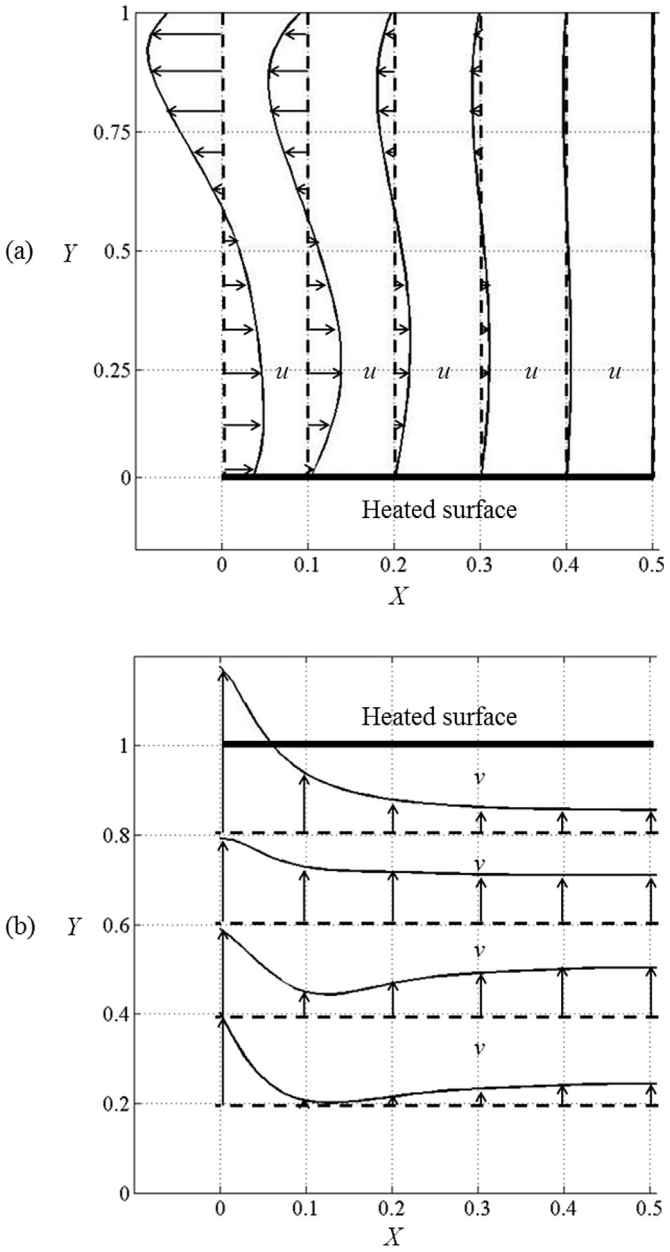

Fig. 14. Velocity profiles at different locations of (a) u along X of [7] and (b) v along Y of present study under $Ra^* = 1.72 \times 10^5$.

5. Conclusions

Natural convection in parallel square plats with a heated top surface is investigated numerically. Results of the present study are quite different from those of the previous study [7], due to the difference of the locations of the heated surfaces. Several conclusions are drawn as follows.

1. Suitability of usage of the combination of the absorbing boundary condition and modified LODI method as the hybrid boundary condition is proven to successfully overcome the problem caused by different directions of the thermal diffusion and mainstream flow in a central low region.
2. Due to the location of the heated top surface, local Nusselt numbers distributed on the top surface form concentric circles.
3. A comparison of the present results with existing experimental results displays a slightly deviation of 10%.

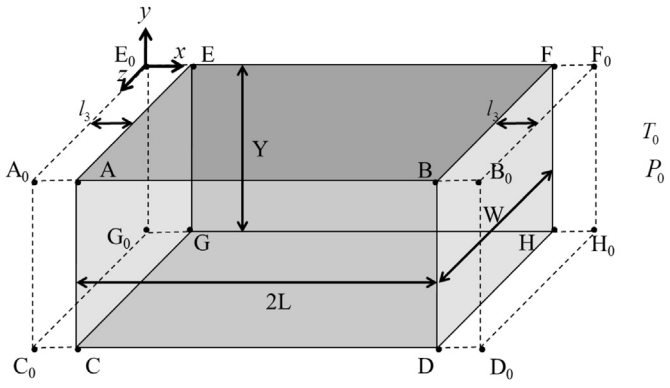

Fig. 15. Physical model for comparing the existing study [16].

Table 1
Computation parameters.

Case	Computation domain grid numbers	Physical domain grid numbers	Ra ($Y/2L$)
1	$100 \times 32 \times 50$	$70 \times 32 \times 50$	2.00×10^2
2	$100 \times 36 \times 50$	$70 \times 36 \times 50$	3.82×10^2
3	$100 \times 40 \times 50$	$70 \times 40 \times 50$	6.69×10^2
4	$100 \times 50 \times 50$	$70 \times 50 \times 50$	2.15×10^3
5	$100 \times 60 \times 50$	$70 \times 60 \times 50$	5.51×10^3
6	$100 \times 70 \times 50$	$70 \times 70 \times 50$	1.20×10^4
7	$100 \times 80 \times 50$	$70 \times 80 \times 50$	2.38×10^4

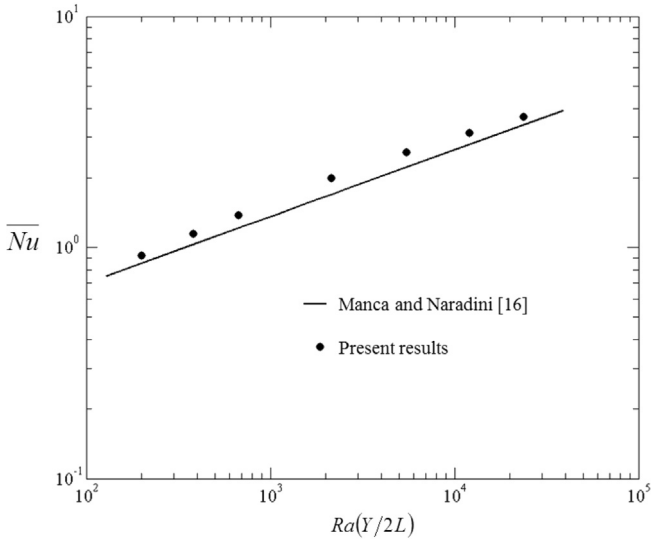

Fig. 16. Comparison of present results and results of Manca and Nardini[16].

Acknowledgment

The authors gratefully acknowledge the support of the Natural Science Council Taiwan under Contract NSC100-2221-E-009-086-MY2.

References

[1] D.D. Gray, A. Giorigini, The validity of Boussinesq approximation for liquids and gases, Int. J. Heat. Mass Transf. 19 (1976) 545–551.
[2] T.J. Poinsot, S.K. Lele, Boundary conditions for direct simulations of compressible viscous flows, J. Comput. Phys. 101 (1992) 104–129.
[3] W.S. Fu, C.G. Li, C.P. Huang, J.C. Huang, An investigation of a high temperature difference natural convection in a finite length channel without Bossinesq assumption, Int. J. Heat. Mass Transf. 52 (2009) 2571–2580.
[4] W.S. Fu, C.G. Li, C.C. Tseng, An investigation of a dual-reflection phenomenon of a natural convection in a three dimensional horizontal channel without Boussinesq assumption, Int. J. Heat. Mass Transf. 53 (2010) 1575–1585.
[5] C. Yoo, Y. Wang, A. Trouvé, H. Im, Characteristic boundary conditions for direct simulations of turbulent counterflow flams, Combust. Theory Model. 9 (4) (2005) 617–646.
[6] G. Lodato, P. Domingo, L. Vervisch, Three-dimensional boundary conditions for direct and large-eddy simulation of compressible viscous flows, J. Comput. Phys. 227 (2008) 5105–5143.
[7] W.S. Fu, W.H. Wang, C.C. Li, S.H. Huang, An investigation of natural convection in parallel square plates with a heated bottom surface by an absorbing boundary condition, Int. J. Heat. Mass Transf. 56 (2013) 35–44.
[8] J.P. Berenger, A perfectly matched layer for the absorption of electromagnetic waves, J. Comput. Phys. 114 (1994) 85–200.
[9] F.Q. Hu, On absorbing boundary conditions of linearized Euler equations by a perfectly matched layer, J. Comput. Phys. 129 (1996) 01–219.
[10] F.Q. Hu, On Perfectly Matched Layer as an Absorbing Boundary Condition, 1996, pp. 96–1664. AIAA Paper.
[11] F.Q. Hu, A stable perfectly matched layer for linearized Euler equations in unsplit physical variables, J. Comput. Phys. 173 (2001) 55–480.
[12] S. Ta'asan, D.M. Nark, An absorbing buffer zone technique for acoustic wave propagation, in: AIAA Aerospace Sciences Meeting and Exhibit, 1995.
[13] B. Wasistho, B.J. Geurts, J.G.M. Kuerten, Simulation techniques for spatially evolving instabilities in compressible flow over a flat plate, Comput. Fluids 26 (7) (1997) 13–739.
[14] J.B. Freund, Proposed inflow/outflow boundary condition for direct computation of aerodynamic sound, AIAA J. 35 (4) (1997) 40–742.
[15] Ali Mani, Analysis and optimization of numerical sponge layers as a non-reflective boundary treatment, J. Comput. Phys. 231 (2012) 704–716.
[16] O. Manca, S. Nardini, Experimental investigation on natural convection in horizontal channels with the upper wall at uniform heat flux, Int. J. Heat. Mass Transf. 50 (2007) 1075–1086.
[17] J. Dennis, P. Thomas, B. Pieter, Recent enhancements to overflow, in: Aerospace Sciences Meeting and Exhibit, 35th, Reno, NV, 1997.
[18] P.L. Roe, Approximation Riemann solver, parameter vectors, and difference schemes, J. Comput. Phys. 43 (1981) 357–372.
[19] J.M. Weiss, W.A. Simth, Preconditioning applied to variable and constants density flows, AIAA J. 33 (1995) 2050–2056.
[20] S. Yoon, S. Jameson, Lower-upper symmetric-Gauss-Seidel method for the Euler and Navier–Stokes equations, AIAA J. 26 (1988) 1025–1026.
[21] I. Abalakin, A. Dervieux, T. Kozubskaya, A Vertex Centered High Order MUSCL Scheme Applying to Linearized Euler Acoustics, INRIA, 2002. No. 4459.